NANOROBOTS

Reconfigurable nanomaterials folded from multicomponent chains of DNA origami voxels

Minh Tri Luu[1,2,3,4], Jonathan F. Berengut[1,4,5,6], Jiahe Li[1], Jing-Bing Chen[1], Jasleen Kaur Daljit Singh[1,3,4], Kanako Coffi Dit Glieze[1,4], Matthew Turner[1], Karuna Skipper[1,4], Sreelakshmi Meppat[1,4], Hannah Fowler[7], William Close[8], Jonathan P. K. Doye[7], Ali Abbas[3,4], Shelley F. J. Wickham[1,2,4]*

In cells, proteins rapidly self-assemble into sophisticated nanomachines. Bioinspired self-assembly approaches, such as DNA origami, have been used to achieve complex three-dimensional (3D) nanostructures and devices. However, current synthetic systems are limited by low yields in hierarchical assembly and challenges in rapid and efficient reconfiguration between diverse structures. Here, we developed a modular system of DNA origami "voxels" with programmable 3D connections. We demonstrate multifunctional pools of up to 12 unique voxels that can assemble into many shapes, prototyping 50 structures. Programmable switching of local connections between flexible and rigid states achieved rapid and reversible reconfiguration of global structures in three dimensions. Multistep assembly pathways were then explored to increase the yield. Voxels were assembled via flexible chain intermediates into rigid structures, increasing yield up to 100-fold. We envision that foldable chains of DNA origami voxels can achieve increased complexity in reconfigurable nanomaterials, providing modular components for the assembly of nanorobotic systems with future applications in synthetic biology, assembly of inorganic materials, and nanomedicine.

INTRODUCTION

A key goal in molecular robotics is to build synthetic systems approaching the complexity of the molecular machines found in living cells, with emergent functions such as chemotaxis and adaptation (*1*, *2*). The fundamental challenge is to achieve efficient self-assembly with high stability while also allowing for rapid transitions between different states and functions. Synthetic self-assembly has achieved important advances, including supramolecular switches and materials (*3*, *4*), de novo design of proteins (*5*, *6*), and functional molecular devices and crystals made from DNA (*7*–*12*). However, many biologically inspired self-assembly strategies are yet to be fully explored. Biology exploits multifunctionality, from the pluripotency of stem cells at the macroscale to the reuse of protein motifs at the molecular level (*13*). Properties such as funnel-shaped energy landscapes, local-to-global folding processes, and the use of molecular chaperones that prevent aggregation have been proposed to explain the folding efficiency of native protein machinery (*14*–*16*). Similarly, recent theoretical models predict that local-to-global folding of linear chains could provide an effective strategy for molecular robotics (*17*).

DNA is an excellent material for self-assembly of nanostructures because of its sequence-specific binding and ease of both synthesis and chemical modification. Diverse self-assembly principles have been demonstrated with DNA, including algorithmic self-assembly (*18*, *19*), hierarchical assembly (*20*–*23*), controlled nucleation of shapes (*24*), pathways (*25*) and microscale structures (*26*), allosteric shape change propagated across structures (*27*), paper folding (*28*), molecular transport (*12*), self-limiting growth (*29*, *30*), and crystal growth to macroscale structures with nanoscale features (*7*, *11*).

One of the most robust and frequently used approaches is the DNA origami method (*31*, *32*), where a long single-stranded DNA (ssDNA) scaffold is folded into diverse nanostructures cross-linked by short ssDNA staple strands to form double-stranded DNA. DNA origami nanostructures provide a three-dimensional (3D) molecular canvas or "pegboard" of addressable pixels that allow for the spatial arrangement of guest molecules (*11*, *20*, *21*, *26*, *33*–*36*) and reconfigurable interfaces for dynamic shape transformation (*8*–*12*, *20*–*22*, *26*–*28*, *33*, *34*, *36*–*42*). However, scaling up DNA nanostructures in size and complexity is essential for advanced applications and is limited by the finite length of the scaffold strand [<10,000 nucleotides (nt)] used in DNA origami, typically derived from the ssDNA genome of the M13 bacteriophage.

Hierarchical assembly of DNA origami subunits is a potential solution to scaffold size limits but is hampered by low yields in two dimensions (*20*, *28*), lack of rigidity in three dimensions (*22*, *26*, *42*, *43*), the high cost of many unique DNA strands (*44*), and laborious processes to achieve different shapes such as redesign (*29*), reassembly (*26*), or stepwise remixing (*20*) of components. Many current approaches also rely on fixed binding interactions between subunits with a high degree of stability (*20*, *21*, *26*), whereas reconfiguration typically requires flexible elements and reprogrammable interfaces (*28*, *37*–*39*).

Here, we present a set of 3D DNA nanostructure "voxels" with internal and external connections that can be switched between inactive, rigid, and flexible states. DNA voxels were combined to form a multipurpose pool of components for assembly of diverse 2D and 3D hierarchical assemblies without redesign, refolding, or remixing of voxels. We then used the DNA voxels to achieve fast and reversible reconfiguration and explore stepwise assembly pathways

[1]School of Chemistry, University of Sydney, Sydney, NSW 2006, Australia. [2]School of Physics, University of Sydney, Sydney, NSW 2006, Australia. [3]School of Chemical and Biomolecular Engineering, University of Sydney, NSW 2006, Australia. [4]University of Sydney Nano Institute, University of Sydney, Sydney, NSW 2006, Australia. [5]EMBL Australia Node for Single Molecule Science, School of Biomedical Sciences, University of New South Wales, Sydney 2052, Australia. [6]ARC Centre of Excellence in Synthetic Biology, University of New South Wales, Sydney, Australia. [7]Physical and Theoretical Chemistry Laboratory, Department of Chemistry, University of Oxford, Oxford, UK. [8]Australian Centre for Microscopy & Microanalysis, University of Sydney, Sydney, NSW 2006, Australia.
*Corresponding author. Email: shelley.wickham@sydney.edu.au

involving folding of flexible DNA voxel chains to improve assembly yield (Fig. 1A).

RESULTS

Construction of rigid DNA origami voxels

The hierarchical DNA origami assembly system described here was based on an existing DNA barrel design (*21*). The barrel was selected because it is rigid and has a high yield, does not form nonspecific aggregates through DNA blunt-end stacking, can polymerize along its coaxial axis, and can be used to template other materials on both inside and outside surfaces (*21*, *33*, *45*, *46*). Here, we extended this design by using a monomer composed of two barrel subunits folded from the same scaffold and linked by a flexible scaffold tether between the top of each barrel. The monomer has 12 external interfaces for connections to tile 3D space (Fig. 1B). Each barrel forms an addressable voxel in the 3D superstructure that can be specifically modified to host different molecular guests.

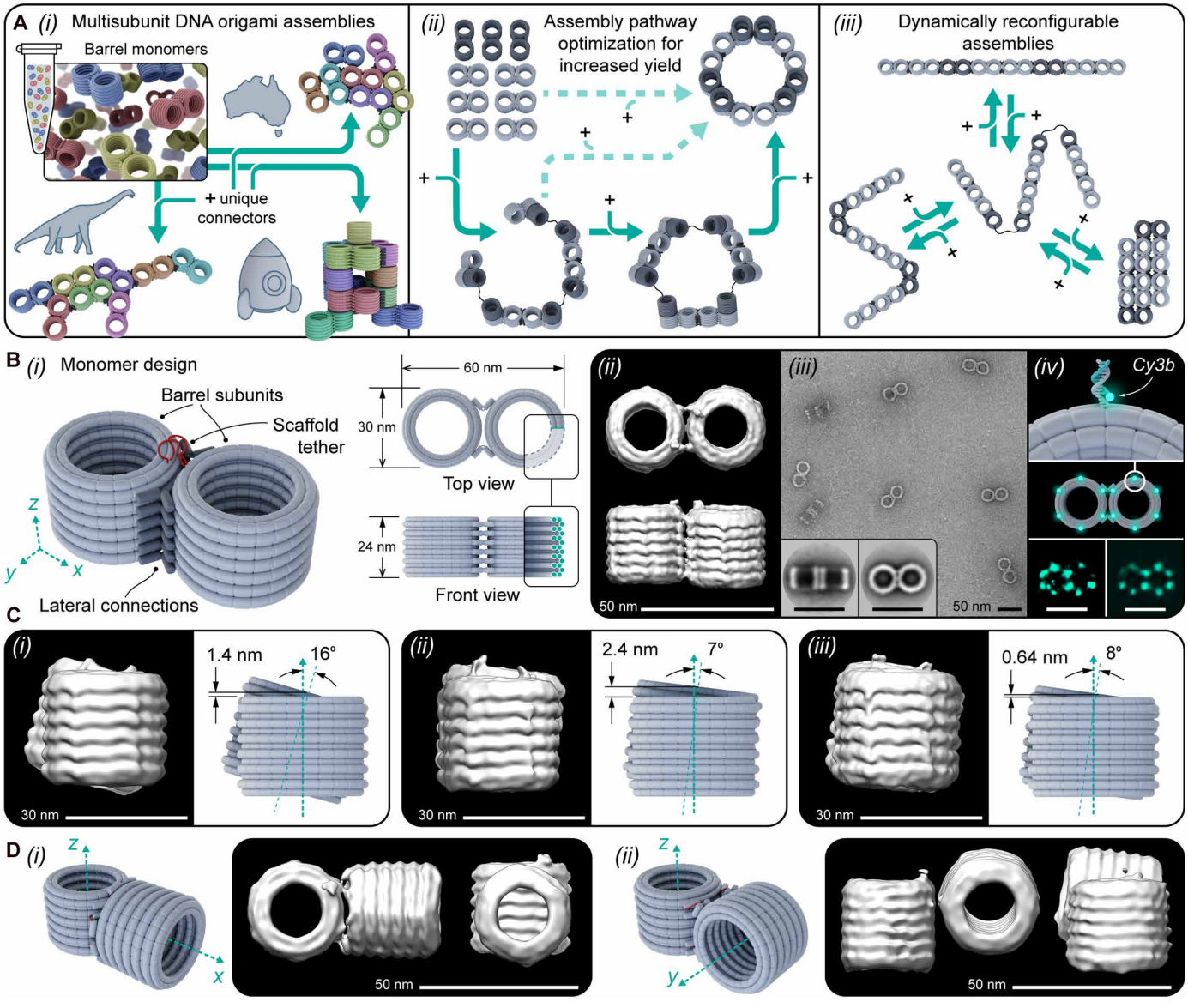

Fig. 1. DNA origami monomers consist of two barrels, or voxels, linked together by rigid or flexible connections. (**A**) (i) Multiple shapes can be assembled from the same monomer pool by adding different unique sets of ssDNA connector strands, (ii) sequential addition of connector strands guides assembly pathways, and (iii) TMSD of connector strands triggers dynamic reconfiguration. (**B**) (i) DNA origami monomer showing rigid intramonomer connections (dark gray) and flexible scaffold tether (red), (ii) cryo-EM reconstruction ($n = 3449$), (iii) TEM and 2D class averages ($n_{front} = 112$ and $n_{top} = 166$), and (iv) DNA-PAINT reconstruction [top and middle: 12 docking strands hybridize fluorophore-labeled imager strands; bottom: example particle (left) and average (right; $n = 10$)]. (**C**) Cryo-EM reconstructions ($n = 7125$, 3647, and 3449; GSFSC resolution = 17.88, 17.83, and 19.25 Å, respectively) show that (i) inward hinges resulted in 16° twist, (ii) horizontally alternating inward and outward hinges reduced twist but increased vertical offset to 2.4 nm, and (iii) vertically alternating inward and outward hinges gave the lowest twist (8°) and offset (0.64 nm). (**D**) Cryo-EM reconstruction of alternative intramonomer interface designs with coaxial axes in (i) *z*-*x* and (ii) *z*-*y* directions ($n = 1999$ and 3928; GSFSC resolution = 18.54 and 23.5 Å, respectively). Scale bars, 30 nm [in (C)] and 50 nm (all others).

Intramonomer lateral connections between barrels were formed by ssDNA "connector" strands that hybridized to ssDNA "plugs" extending laterally from the side of each barrel, cross-linking the two barrels (Fig. 1B and figs. S1 and S2). The interface consisted of 24 7-nt plugs arranged in two vertical arrays with ~15-nm spacing (fig. S3). Connectors consisted of domains complementary to plugs on adjacent barrels separated by a 4-thymine (T) spacer or "hinge." All 24 plug sequences were unique, and each interface had 12 unique 32-nt connector strands. Plug sequences were randomly generated with an average guanine-cytosine (GC) content of 50% and outliers in high or low binding energy removed (fig. S4) (*21*, *26*).

Negative-stain transmission electron microscopy (TEM), cryo–electron microscopy (cryo-EM) single-particle analysis, and DNA point accumulation for imaging in nanoscale topography (DNA-PAINT) were used to confirm the monomer structure (Fig. 1B and table S1). TEM 2D class averages resulted in monomer dimensions of 28 ± 1 nm (width) by 56 ± 1.5 (length) nm by 19 ± 3 (height) nm (fig. S5), in good agreement with design dimensions of 30 nm by 60 nm by 24 nm estimated using the caDNAno software (helix width, 2 nm; 0.34 nm/base pair) (*47*). Measured spacing of docking sites in DNA-PAINT particle averages was 15 ± 0.7 nm ($n = 5$), in agreement with a design spacing of 15 nm (fig. S6).

Cryo-EM reconstructions revealed unintended translational and rotational shifts between the two subunits of the monomer [Fig. 1B (ii) and figs. S7 to S9; gold-standard Fourier shell correlation (GSFSC) resolution of 17.83 to 19.25 Å]. Coarse-grained simulations using oxDNA (*48*, *49*) predicted that this twist was caused by the connectors forming straight helices instead of bent hinges (figs. S10 and S11 and table S1). To cancel out the twist, we introduced connectors with different hinge directions. Inward hinges have the 4-T hinge linker joining the two plugs closest to the center of the interface, as in Fig. 1B. Outward hinges have the 4-T hinge linker joining the two plugs farthest from the interface (fig. S2). Vertically alternating hinge directions in each helix layer of the interface was found to result in the smallest twist and vertical shift between the monomer subunits [Fig. 1C (iii), supplementary discussion S1, and fig. S8]. Alternative monomer geometries were also developed where the coaxial axes of the barrel subunits point in different directions, *z-y* and *z-x* (Fig. 1D and figs. S12 to S14).

Multicomponent lateral and coaxial assembly of voxels

Voxels were assembled via intermonomer lateral and coaxial connections (Fig. 2, A and B). Unique monomers (Fig. 1A, colors) were defined by 96 unique lateral plug sequences and 72 unique coaxial plug sequences (1212 nt), whereas core DNA sequences were repeated (8952 nt, 88%). This approach allowed for efficient reuse of many core strands in all monomers (4848 nt, 49%). Voxels were folded in separate reactions, allowing for fully addressable modification of both interface and core sequences during monomer folding. Lateral connections were based on the intramonomer design (Fig. 2A and fig. S15), whereas coaxial connections were based on previously published designs (*21*) (Fig. 2B and fig. S16).

Connector strands were designed to successfully assemble all 14 uniquely identifiable dimers (supplementary discussion S1). Gel analysis was used to quantify dimer band intensity as a fraction of the whole lane intensity, which gave a dimer yield relative to the total amount of monomer added to the assembly reaction (fig. S17). TEM was used to evaluate geometry and rigidity (Fig. 2, A and B, and fig. S18). Purified monomers were used to examine assembly and reconfiguration processes because this allowed for unambiguous identification of assembly defects. Overall yields relative to the amount of M13 scaffold added were expected to be lower to account for monomer folding yield and purification (supplementary discussion S4).

All seven lateral dimers had high relative yields (81 to 91%), whereas yields for the seven coaxial dimers were slightly lower (45 to 86%) and depended on the connector sequence set (fig. S19). Using two coaxial connection sets instead of one increased the yield, for example, from 47 to 78% for the lowest yield connector set (fig. S19). Only the target dimer geometry was observed in TEM images for all designs, indicating specificity of barrel connections. Reference-free 2D class averages were generated for TEM images using automated particle selection with no particles discarded, resulting in a small number of classes ($n = 1$ to 3). The fine structural detail visible in the class averages shows particle uniformity and lack of deformation in the dry state, providing evidence of rigidity (Fig. 2A). In some cases, blurred regions of class averages indicate flexibility or instability (e.g., dimer 10; fig. S18).

A detailed analysis of the flexibility of lateral interfaces was performed for the "wave" (dimer 4), comparing one and two vertical connector arrays. The angular spread (Δα; standard deviation, SD) was found to decrease threefold from 15.4° for one array to 5.2° for two, indicating an increase in rigidity (Fig. 2C). The single array had a higher average angle (148°), indicating that the flexible hinge preferred to swing "closed," likely caused by a combination of local blunt-end helix stacking within connectors and steric repulsion between barrels (fig. S10). The precision of rotational shift was further tested for the seven coaxial dimers, in 30° rotation steps (β) from 0° to 180° (Fig. 2D). The observed rotation agreed with designed values, with a low angular spread ($\Delta\beta = 1.1°$ to 9°) indicating rigidity. Lateral and coaxial dimers were also assembled into polymers (figs. S20 and S21). Persistence lengths were estimated as 1044 nm (lateral, width one unit), 1164 nm (lateral, width two units), and 1816 nm (coaxial, width two units) and were comparable to those of four-helix (1000 nm) and six-helix (2030 nm) bundle DNA origami (*50*). Coaxial polymers had a 9° helical twist, in agreement with the 8° intramonomer twist measured by cryo-EM (Fig. 1C).

To enable switching by strand displacement, we designed intramonomer connector strands with additional unique 7-nt toehold domains. "Invader" strands, complementary to both toehold and connector domains, were added to displace connectors by toehold-mediated strand displacement (TMSD) (*51*). Monomers were then in a "free" state where subunits could reorient but remain tethered, allowing different structures to form on addition of alternative connector sets (fig. S22). Invader and alternative connector strands were added simultaneously in one step, and switching yields were high (93 to 97%, 0.5 nM; Fig. 2E and fig. S23). However, at higher monomer concentrations (1 nM), the switching yield decreased to 75% because of increased intermonomer dimerization (25%; fig. S24).

Multifunctional monomer pools for 2D and 3D superstructures

A key goal of our design approach was to exploit the multifunctionality of a single set of monomers to rapidly prototype many different shapes. To start, we initially folded three unique monomers (Fig. 3A)

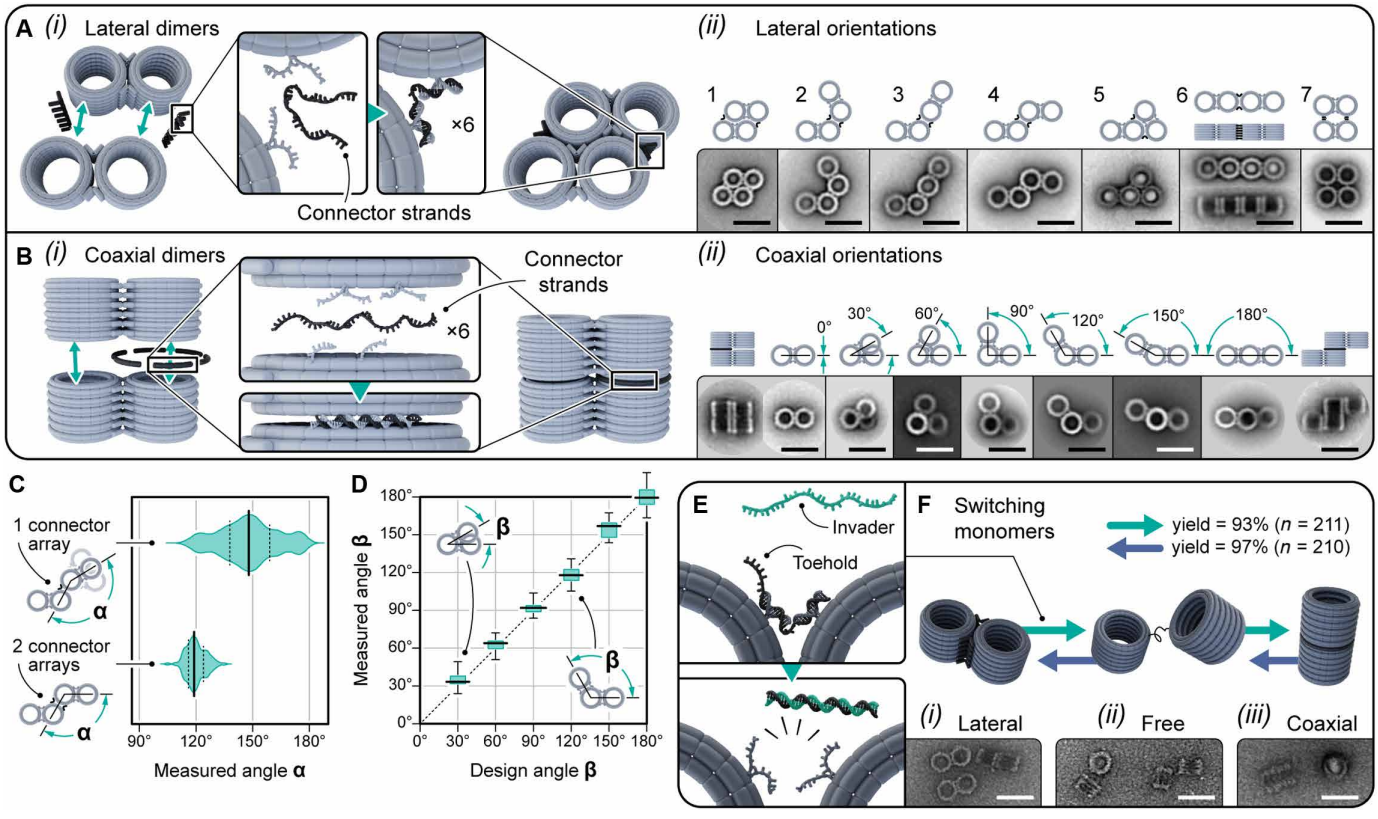

Fig. 2. Programmable rigid connections between monomers. (**A**) (i) Lateral connections in *x-y* were formed by hybridization of connector strands to 7-nt plugs extending from outer helix staples and (ii) seven unique lateral dimers. Top row: 2D models. Bottom row: TEM class averages (left to right: $n = 39$, 90, 37, 110, 24, 72, 30, and 89). (**B**) (i) Coaxial connections in *z* were formed by connector strands hybridizing to plugs extending from middle helix staples and (ii) seven unique coaxial dimers. Top row: 2D models. Bottom row: TEM class averages (from left to right: $n = 58$, 29, 29, 30, 95, 303, 218, 257, and 88). (**C**) Comparison of lateral dimer designs with one or two vertical arrays of connectors; the distribution of angles was smaller for the two-array design, and the one-array design had a larger preferred angle. Angles measured from individual particles in TEM images ($n = 120$ and 103). (**D**) Comparison of design and measured angle of the coaxial dimers in (B), angles measured from TEM particles (left to right: $n = 60$, 37, 41, 31, 18, and 26). (**E**) DNA strand displacement triggered reversible switching of monomers between lateral and coaxial states, with forward and reverse yields of 93 and 97%, respectively. Connector strands have a 7-nt toehold; a one-step process involved simultaneous addition of invader strands to remove existing connectors and the next set of connector strands. Yields were calculated from TEM images. Scale bars, 50 nm.

separately, then combined them into a pool with equal concentrations and purified. The purified pool was divided into subpools, and different connector strand sets were added to successfully construct 17 different trimers (Fig. 3B). Assembly yields determined by gel were high (average 86.1 ± 3.7%; Fig. 3B and fig. S25), and TEM class averages showed accurate shapes formed with good uniformity ($n = 1$ to 4 classes; fig. S26). We found that minimizing the monomer twist (Fig. 1C) was essential to achieving accurate assembly of larger structures (supplementary discussion S1).

To demonstrate increased complexity, we used pools of up to 12 unique monomers to construct arbitrary 2D shapes, including three 8-monomer structures (dinosaur, Australia, and rectangle) and three 12-monomer structures (dragon, robot, and square) (Fig. 3C, supplementary discussion S1, and figs. S27 to S33). It was also possible to form 8-monomer structures, such as the dinosaur, from a 12-monomer pool. TEM images confirmed that the particles had the correct geometry. Generally, the resolution of class averages and hence rigidity was observed to be higher for regions with more adjacent monomers (Fig. 3C). For example, monomers in the dinosaur body were connected to three adjacent monomers and had a high resolution in the class average, indicating rigidity. The head monomer was connected to one adjacent monomer and had a lower resolution, indicating flexibility. Assembly was also possible from unpurified monomer pools, with comparable yields if a correction for the estimated purification losses was included (9 to 53% for 2- to 8-monomer structures; figs. S34 and S35).

In agreement with a previous work on multistep assembly of 2D origami tiles (*20*), a sharp decrease in yield was observed with increasing monomer number, from 78 ± 14 to 36 ± 7% for 3- to 12-monomer structures (Fig. 3D). Addressability of voxels in the resulting hierarchical assembly was confirmed using DNA-PAINT (Fig. 3E). Last, we demonstrated a potential templating application by successfully patterning 10-nm gold nanoparticles inside specific voxels (Fig. 3F).

Multifunctional voxel pools were then used to build more complex 3D shapes. Hollow 3D "boxes" demonstrated cavity size control, a useful feature for templating nanoparticle assembly. Class averages of small and large boxes showed cavity sizes with potential to capture spherical 20- and 40-nm nanoparticles, respectively [Fig. 3G (i and ii) and figs. S36 to S39]. A 3D rocket ship was designed on a hexagonal lattice to test greater asymmetry [Fig. 3G (iii) and fig. S40]. Several design iterations were explored to optimize the

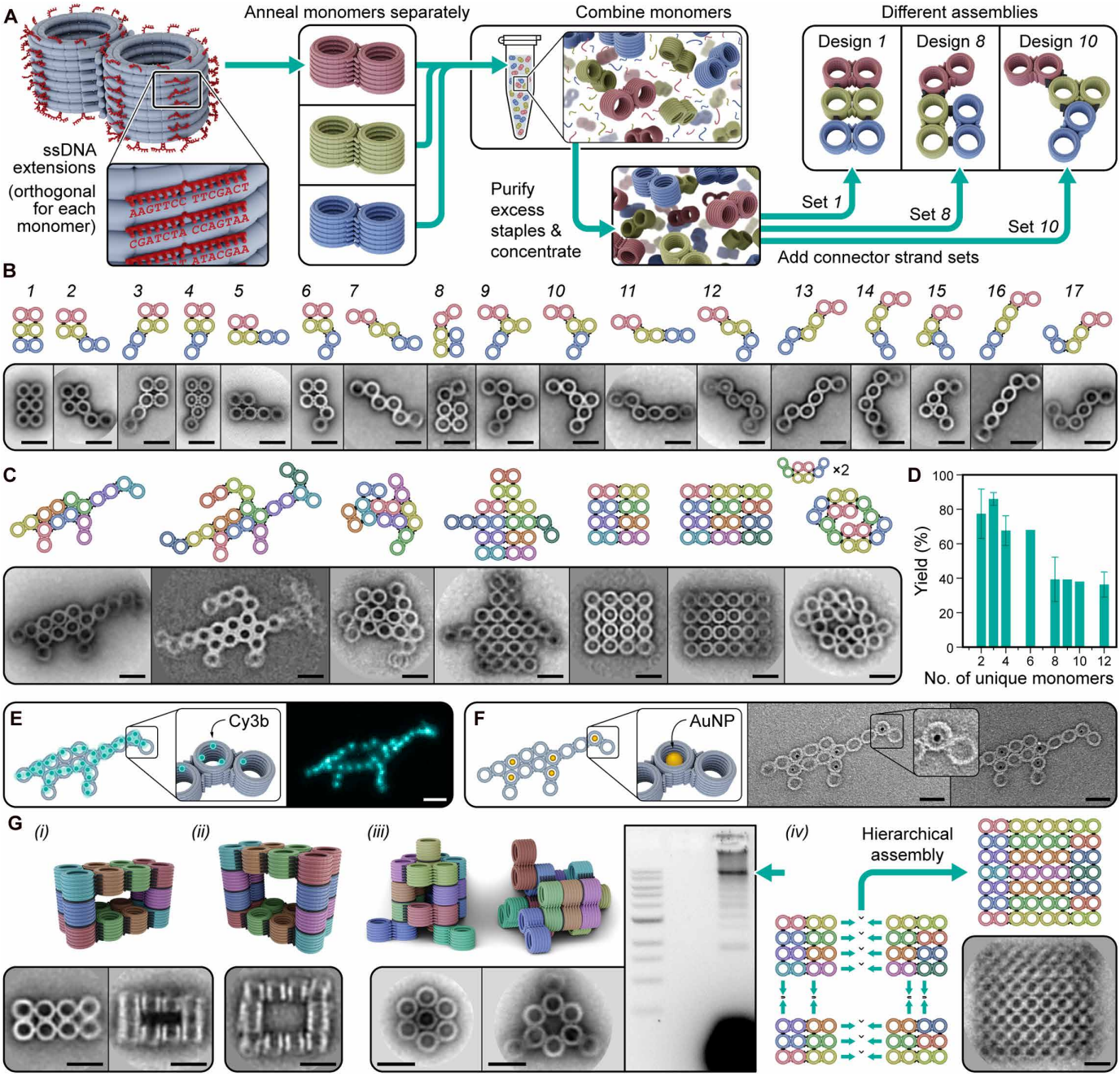

Fig. 3. Multifunctional monomer pools assemble diverse 2D and 3D shapes. (**A**) Workflow to build different shapes from the same set or pool of monomers. Left to right: Unique monomers with unique plug sequences and reused core sequences were folded separately, combined, and purified or concentrated as a monomer pool. The specific connector strand sets added determined the final structure. (**B**) Seventeen trimer assemblies were built from the same trimer pool in (A). Top row: Rendered model. Bottom row: TEM class averages with *n* (left to right) = 133, 74, 73, 82, 31, 99, 48, 51, 21, 38, 32, 32, 43, 38, 46, 36, 34, and 37. (**C**) Models and class averages of larger assemblies built from 8- or 12-monomer pools with *n* (left to right) = 21, 11, 11, 11, 22, 21, and 21. (**D**) Assembly yield decreased with the number of unique monomers, *N* (number of independent designs) = 14, 18, 3, 1, 3, 1, and 6, respectively. (**E**) DNA-PAINT of the dinosaur shape. Left to right: Fully addressable pattern of DNA PAINT docking handles; particle average ($n = 10$). (**F**) Gold nanoparticle patterning. Left to right: Addressable pattern of gold nanoparticles; TEM images. Selected monomers were folded with ssDNA handles on the inner surface to hybridize with ssDNA-conjugated 10-nm gold nanoparticles. (**G**) Scale-up of assembly complexity and size. Model and class average for a (i) small-cavity 3D box ($n = 27$) and (ii) large-cavity 3D box ($n = 10$). (iii) A 12-monomer 3D shape that resembled a rocket. Also shown are TEM class averages of the tip ($n = 16$) and base ($n = 33$) segments and agarose gel electrophoresis results for the entire structure showing the optimized assembly yield of the 12-monomer structure. (iv) Multistep assembly process and class average of 28-monomer rectangle ($n = 25$). In the first stage, monomers were assembled into 8- and 6-monomer squares and rectangles, respectively, and then combined to form a fully addressable 28-monomer rectangle (210 nm by 240 nm by 30 nm), but the yield was too low to measure. Multistep assembly was also used to form an 8-monomer swirl as a homodimer of a 4-monomer "smile" [(C), far right]. Scale bars, 50 nm.

connection pattern and resulted in an increase in yield of the 12-monomer structure from 5 to 33% (gel yield; fig. S41). However, although class averages for subcomponent 4- and 8-monomer rings showed the correct structures by TEM [Fig. 3G (iii) and fig. S42], the complete 12-monomer structure collapsed under dry TEM conditions [Fig. 3G (iii)]. Multistep assembly strategies previously developed (*20*, *52*) were also used to construct a 28-monomer rectangle from two 8-monomer and two 6-monomer oligomer subunits [Fig. 3G (iv) and fig. S43] and a "swirl" by homodimerization of 4-monomer subunits (Fig. 3C and fig. S44).

Dynamic reconfiguration of 2D and 3D voxel assemblies

Dynamic reconfiguration was then explored for 2D and 3D voxel shapes (Fig. 4). Similarly to monomers (Fig. 2E), intramonomer interfaces on "vertex" voxels were switched between flexible and rigid states by addition of invader or connector strands. The length of the ssDNA scaffold tether was found to affect yields of possible monomer geometries (fig. S45). The 354-nt tether has a theoretical maximum ssDNA contour length of ~240 nm, but in oxDNA simulations, the tether was predicted to have secondary structure (fig. S10). Experimentally, structures with tether spacings of 7 to 33 nm formed with high yields ($N_{designs} = 7$, 79 to 89%; figs. S137 and S138). Yields were lower for the 62-nm tether spacing but recovered after addition of short complementary strands to remove secondary structure from the scaffold, increasing the range of possible structural reconfigurations (fig. S46).

An 8-monomer flexible chain with two vertex voxels was used to demonstrate reconfiguration between four shapes with high yield (average 85 ± 5%; Fig. 4, A and B, and figs. S47 to S58). The switching yield for the rod-rectangle transition was measured as a function of time, and ~80% yield was reached in 60 min (Fig. 4C and tables S3 and S4), a timescale comparable to previous origami multimer switching results (*40*). Rate constants were estimated as 1×10^7 and 2×10^7 M^{-1} s^{-1} for forward and reverse transitions, respectively, assuming second-order reactions. Over five complete cycles between the rod (30 nm by 480 nm) and rectangle (90 nm by 180 nm), consisting of 10 total transitions, the yield of the target shape was consistently above 75% (Fig. 4D and tables S5 and S6), demonstrating repeatable high-yield reconfiguration at larger length scales. In contrast, reconfiguration of an equivalent untethered version had 0% yield at the same concentration (0.07 nM) after 18 hours. Even at a much higher concentration (1 nM), the untethered system had an eightfold lower yield (3 to 10%) in 1 hour and remained lower after 18 hours (64 to 77%) (fig. S57). Reconfiguration of this structure was also used to drive rearrangement of a 20-nm gold nanoparticle cargo (Fig. 4H and fig. S59). This resulted in gold pattern transition from a symmetric design with 30-nm center-to-center spacing (rectangle) to an asymmetric design with 150- and 210-nm spacing (rod).

We then explored more diverse structural reconfigurations with a closing circular aperture (Fig. 4E) and a transition between a 1D rod and a 3D box with cavity (Fig. 4G). The 9-monomer 3D circle was designed with two layers to incorporate both lateral and coaxial connections for greater reconfiguration options. Local-to-global reconfiguration was then tested for the circle to achieve reversible closing and opening of the central aperture. The flexible cyclized structure (Fig. 4E, top) was used as a transitional structure, and vertex monomers (dark gray in Fig. 4E and fig. S60) were switched between 0°, 60°, and 180°. At the same time, the intermonomer interfaces were switched between concave, straight, and convex states (Fig. 4E, inset). This resulted in reconfiguration between the compact triangle, equilateral triangle, and circle (Fig. 4E). Correct switching was confirmed by TEM for one-step transitions (flexible-to-rigid and rigid-to-flexible) and for an example two-step reconfiguration pathway (flexible-compact-flexible-circle) (figs. S61 to S63). Last, a 12-monomer flexible voxel chain was reconfigured between a 1D rod and the 3D voxel box with cavity from Fig. 3G, with 96% yield (Fig. 4, F and G, and figs. S64 and S65).

Improving assembly yield by folding monomer chains

Our results (Fig. 3D) showed decreasing yield with increasing monomer number, limiting potential applications. Possible causes of low yields include incorrect monomer stoichiometry, aggregation due to nonspecific interactions between the large number of randomly generated connector sequences, and kinetic traps in assembly pathways (supplementary discussion S3). In comparison, assembly methods that control nucleation have achieved assembly of defined shapes of >1000 DNA origami slats into 2D shapes (*26*), and seeded assembly methods have achieved sophisticated algorithmic control of DNA tile assembly (*18*, *19*). Here, we observed that, for a given monomer number, some designs had higher yields (Fig. 3D), and monomer reconfiguration had high yields (93 to 97%; Fig. 2E). This suggested that assembly paths with efficient transitions between high-yield intermediate or "precursor" structures may improve yield. We explored this concept for three designs: a 12-monomer 3D box, an 8-monomer 2D rectangle, and a 9-monomer circle (Fig. 5).

Two structures with high reconfiguration yields were the 3D box (Fig. 2, F and G; 96%) and 2D rectangle (Fig. 4, A to D; >80%). The yields of target shapes were then determined for different assembly pathways (Fig. 5, A and B). For the 3D box, two designs with different arrangements of intra- and intermonomer connections were compared (figs. S66 to S70). A "stacked" design with parallel lateral intramonomer connections had a higher yield (24%) in direct assembly than an "offset" design, with staggered lateral and coaxial intramonomer connections (3%) (Fig. 5A). The lower yield of the offset design was potentially due to the greater flexibility of local connections (fig. S69). However, the offset assembly yield increased ~11-fold for a three-step pathway with a 1D rod and flexible chain intermediates (3 to 35%). This resulted in a higher final yield than for direct assembly of the stacked design (24%) (Fig. 5A). The stacked design could not achieve the same three-step pathway because the pattern of intermonomer interfaces was not compatible with forming a 1D rod. Similarly, the highest yield for the 2D rectangle was achieved via a three-step pathway beginning with a 1D rod, but the yield increase here was more modest (1.4-fold, 48 to 68%; Fig. 5B and fig. S71).

The 9-monomer 3D circle had the lowest direct assembly yield of any structure tested (gel yield < 0.4%; Fig. 5C and fig. S72), with no correct circles found in TEM images. Instead, images of direct assembly products showed spiral polymers [Fig. 5C (ii) and fig. S73]. The single-array interfaces used in the circle were found to have a preferred angle of 150° ± 15° in dimers (Fig. 2C), but here, they were required to form a 120° angle, potentially leading to strain that inhibited ring closure. Insights from supramolecular chemistry suggested that a high monomer concentration would benefit intermonomer bonds forming (state 0-1), whereas a low chain concentration would benefit intrachain bonds forming (state 1-2). A benefit of multiple assembly steps was that reaction conditions could be optimized independently. Thus, a flexible

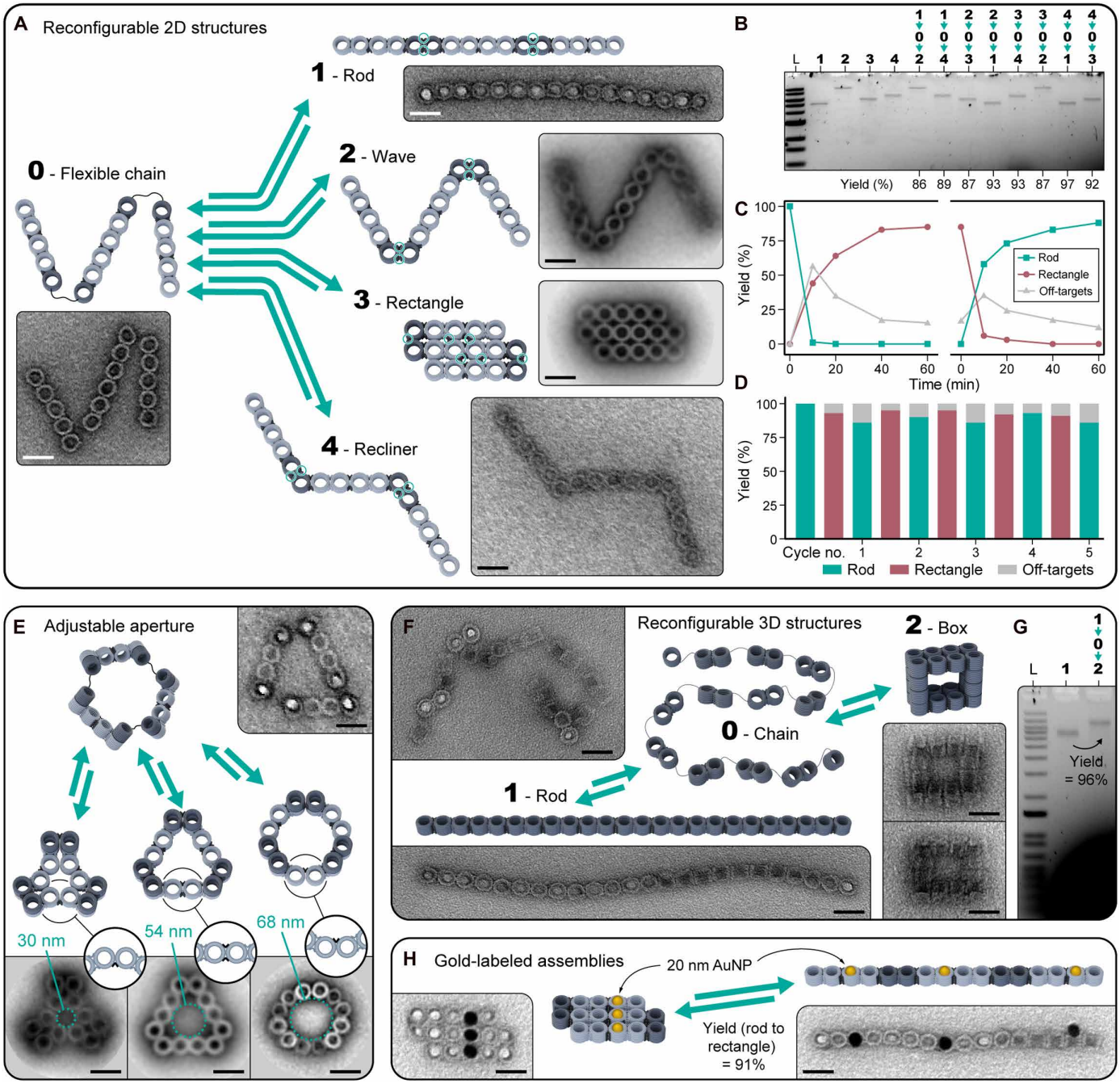

Fig. 4. Programmable reconfiguration of DNA origami voxel chains in 2D and 3D. (**A** to **D**) An 8-monomer flexible voxel chain (state 0) was switched between extended 1D and compact 2D states; numbers 1 to 4 indicate possible final states of the system. (A) Left: TEM image of the flexible chain (state 0, $n = 1$). Right, top to bottom: TEM image of linear rod (state 1, $n = 1$), wave (state 2, $n = 30$), rectangle (state 3, $n = 111$), and recliner (state 4, $n = 1$). To reconfigure between states (blue arrows), we added invader and connector strands to disrupt key interfaces (blue circles) and form the next structure. (B) Agarose gel analysis of switching reactions for pairwise transitions between states for the flexible chain at 37°C. Invaders and connectors were added sequentially in this example so that sequences could be reused. Reconfiguration direction depended on the input signal, e.g., 1-0-2 or 2-0-1. (C) Switching yield as a function of time at 40°C for the rod-to-rectangle pathway (i) and reverse (ii) from TEM images. In this example, invaders and connectors were added simultaneously given that no sequences were being reused. (D) Switching yield for 10 consecutive steps (five cycles) at 40°C from TEM statistics ($n_{average} = 147$). As the number of cycles increased, higher concentrations of connectors and invaders needed to be added to achieve consistent yields. Scale bars, 50 nm. (**E**) A 9-monomer DNA voxel ring was reconfigured into three different shapes with central aperture diameters from 30 to 68 nm. Top: TEM image of the flexible ring. Bottom, left to right: TEM class average of compact triangle, equilateral triangle, and circle ($n = 23$, 90, and 24). (**F** and **G**) TEM (F) and agarose gel (G) of a 12-monomer flexible voxel chain (state 0, $n = 1$) that was reconfigured between a 1D rod (state 1, $n = 1$) and a 3D voxel box with cavity (state 2, $n = 1$, same design as in Fig. 3G). The gel yield was 96%. State numbers here refer to substates of the 3D box transition, which are distinct from those in (A) to (D) for the rectangle transition. (**H**) Voxel reconfiguration achieved rearrangement of a gold nanoparticle cargo. 1D to 2D reconfiguration from (A) including three voxels decorated with 20-nm gold nanoparticles resulted in a gold pattern transition. Yield was 91% for rod to rectangle (TEM, $n = 114$). Yield calculations for (B) and (G) were by gel, and those for (C), (D), and (H) were by TEM. Scale bars, 50 nm.

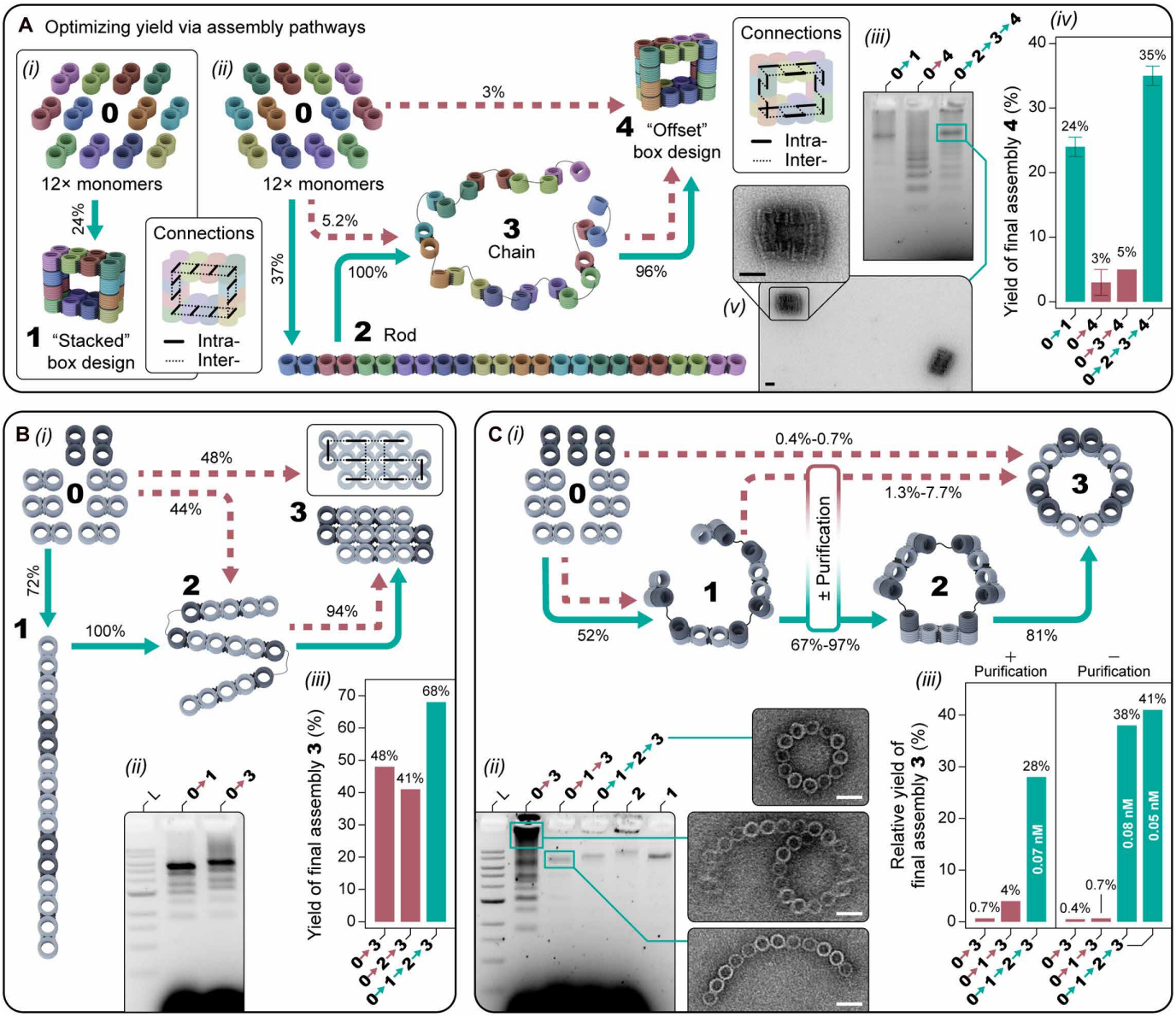

Fig. 5. Folding DNA origami voxel chains to direct assembly pathways and increase the yield. Assembly yields for different design pathways, relative to the amount of prepurified monomer, were determined by agarose gel by quantifying target band intensity over total lane intensity (iii and iv), with correct target bands confirmed by TEM (v) (supplementary discussion S4). State numbers are reused for each design set, keeping state 0 as the monomer pool for all examples. (**A**) Yield of the 12-monomer 3D box design [from Fig. 3G (ii)] depended on the monomer arrangement. (i) A stacked design, with parallel lateral intramonomer connections, had a higher yield in direct assembly (state 0-1) than (ii) an offset design, with staggered lateral and coaxial intramonomer connections (state 0-4). The offset design could also be assembled via the high-yield intermediate rod (as in Fig. 4F), given that it required only lateral intermonomer connections. The multistep assembly pathway (state 0-2-3-4) gave the overall highest yield for the 3D box. The stacked box could not be formed from the rod intermediate because it required both coaxial and lateral intermonomer connections. (**B**) (i to iii) Similarly, multistep assembly resulted in a higher yield of the 8-monomer 2D rectangle (from Fig. 4A) when assembled via the rod intermediate (state 0-1-2-3) than either direct assembly (state 0-3) or via a flexible chain (state 0-2-3). (ii) Increased yield was likely due to lower amounts of high–molecular weight aggregates seen in folding gels for direct assembly of the rod (state 0-1) compared with the rectangle (state 0-3). (**C**) (i to iii) For the 9-monomer 3D circle (from Fig. 4E), direct assembly resulted in essentially zero yield (state 0-3), and spiral aggregates were observed by gel and TEM instead (ii). Assembly via a flexible chain (state 0-1-3) also gave low yield of closed rings, and TEM images showed open curves instead. Addition of an extra "flexible ring" intermediate (state 0-1-2-3) increased the circle yield 100-fold, suggesting that monomer orientations in the final circle design introduced strain that inhibited ring closing. Introduction of a purification step for flexible chains increased the three-step assembly yield (state 0-1-3) but decreased the four-step assembly yield (state 0-1-2-3). An optimal assembly yield from monomers to the final shape was 100-fold higher for the path with the most sequential steps (0-1-2-3) without intermediate purification.

chain was selected as a high-yield precursor, with higher-yield double-array intermonomer connections and flexible intramonomer tether connections (Fig. 5C).

The flexible linear chain was first assembled at a high monomer concentration (1 nM per monomer), resulting in a high yield [52 ± 5%; Fig. 5C (ii) and fig. S74]. Unpurified or gel-purified chains

were then folded into circles at low concentration (0.05 to 0.08 nM) and classified by TEM (figs. S75 and S76). Although the assembly yield increased sixfold, it remained low (4%, gel-purified chain). TEM images showed that polymerization was avoided, but most circles failed to close (fig. S73). Thus, a further intermediate step of a flexible cyclized triangle was added [Fig. 5C (ii)], in which the stronger double-array interfaces were proposed to template ring closure. Last, the flexible intramonomer tethers were then switched to rigid connections, and the double-array intermonomer connections were removed to form single-array connections. Compared with direct assembly, the longest pathway involving two intermediate states resulted in up to a 100-fold increase (unpurified chains, 0.4 to 41%, gel yield) with a 40-fold increase for purified chains [0.7 to 28%, TEM yield, excluding the yield of the purification step; supplementary discussion S4, Fig. 4A (iii), figs. S77 to S80, and table S2]. Lower yields observed for purified chains were likely due to a combination of damage during purification and incomplete separation of 9-monomer structures from 8-monomer structures, given that many truncated chains were observed in TEM images (table S2).

DISCUSSION

Although custom multicomponent DNA origami assemblies can be designed with high precision for specific functions, such as rotary molecular motors (*10*) or multimaterial lattices (*11*), our multipurpose voxel pools allow for more rapid prototyping of diverse shapes for different applications. Many applications require optimization of geometric parameters such as cavity size, packing geometry, and rigidity at sizes greater than achieved by a single M13 scaffold (10 to 100 nm). For example, to build DNA-templated inorganic crystals with dynamic optical properties requires optimization of cavity size to host nanoparticles >50 nm for strong plasmonic effects and with periodicity on the order of the wavelength of light (200 to 800 nm) for photonic applications. Another important application area for multicomponent DNA origami systems is as scaffolds for biophysical studies of large-scale protein assemblies approaching the cell size (1 to 10 μm), such as chemotaxis arrays and the cytoskeleton. To mimic and study these biological systems, the DNA scaffolds must combine high-yield assembly with rapid and efficient dynamic reconfiguration. An advantage of our design is that tethers keep monomers in proximity, allowing for very high reconfiguration yields for voxel chains. We have shown that small local changes in geometry can achieve rapid changes in global structure on timescales suitable for driving the reconfiguration of protein arrays in single-molecule biophysical experiments.

The foldable DNA voxel chain provides a prototyping system to rapidly explore a range of self-assembly strategies inspired by protein folding and supramolecular chemistry. We show that assembly pathways with high-yield intermediate states were able to rescue a 3D circle design from essentially zero yield to a usable yield. This system has future applications in exploring how strategies such as sequential reduction in conformational freedom, templating, and reuse of functional motifs can be useful in multicomponent origami assembly. In particular, longer foldable voxel chains could be folded into complex shapes, analogous to the way the ssDNA scaffold can be folded into DNA origami shapes (*17*). Recent works are only just beginning to elucidate the kinetics of DNA origami folding (*53*, *54*). In the future, insight into DNA origami folding mechanisms can also be applied to designing optimal assembly pathways for DNA origami chains. DNA voxel chains can also be used to explore whether it is possible for 3D origami chain displacement to overcome steric barriers to mimic DNA strand displacement, similar to 1D nanorod (*22*) or 2D tile displacement (*38*), to incorporate dynamic computing. There is potential to incorporate principles of algorithmic self-assembly to achieve further structural diversity with the same set of 12 voxels (*18*).

Some limitations to this approach include the large number of unique connector strands, low concentration assembly conditions, and compatibility with physiological conditions. Future sequence optimization, for example, to maximize the Hamming distance (*26*), has the potential to improve the yield further by decreasing nonspecific interactions and to reduce the number of unique connector strands, allowing scale-up of a unique voxel number and decreasing cost. Current methods of yield analysis, gel densitometry, and TEM have systematic errors and low accuracy. More accurate methods to quantify yield and quality would allow for more precise optimization of assembly parameters (*55*). It is possible that assembly concentrations for folding DNA chains can be further optimized for increased yield, although there will be a practical limit to dilution for ease of handling samples and utility in downstream applications. Dilution was particularly important for ring closure, and the closure rate is expected to decrease with increasing chain length. Thus, larger rings or wireframe structures may require templating to close. Alternative approaches to dilution could include solid-phase assembly or systems that mimic protein chaperones, which act in part by sequestering amino acid chains to prevent multimolecular aggregation during protein folding (*16*). The current system can switch at 37°C (Fig. 4B), and reconfiguration of DNA origami chains occurs within minutes at very low concentrations, which opens up future uses as responsive components of synthetic biological systems. However, this system is not compatible with physiological buffers and would need to be stabilized with protective coatings such as oligolysine–polyethylene glycol (PEG) (*56*). A recent work has shown that ssDNA handles attached to the surface of DNA origami structures remain addressable after coating (*57*), suggesting the potential for coated structures to undergo reconfiguration.

In conclusion, we have described multipurpose pools of DNA origami voxels that serve to rapidly prototype dynamic 3D multicomponent DNA origami nanostructures. The voxels retain a regular arrangement of addressable surface sites and are able to reconfigure guest molecules, such as gold nanoparticles, with high precision between complex patterns. Interfaces are optimized for both high-yield, high-stability assembly and rapid dynamic reconfiguration and could be adapted to respond to more varied inputs, including pH, small molecules, and external electric and magnetic fields. Last, our foldable DNA voxel chains achieved increased yield by optimizing assembly pathways. Together, these results represent a substantial step toward achieving adaptive molecular robotic systems by providing nanoscale components with programmable and reliable actuation with many degrees of freedom. In the future, we envision that foldable chains of DNA origami voxels could be integrated with molecular sensing and information processing systems (*18*) and with top-down lithographic nanofabrication methods (*41*) to achieve increased levels of functionality (*33*, *34*, *42*, *58*). This has the potential to open up future applications in nanorobotics, such as environmentally responsive optical and magnetic materials, automated nanorobotic assembly lines for custom assembly of nano- and

microscale materials on demand, and adaptive nanomachines that can operate in physiological environments for nanomedicine.

MATERIALS AND METHODS

Folding of DNA origami voxels

All chemicals were purchased from Sigma-Aldrich unless otherwise noted. DNA strands were purchased from IDT (Integrated DNA Technology) and resuspended in Milli-Q water to a minimum concentration of 200 μM. Monomers were folded from a 7308-nt ssDNA M13 scaffold (Guild BioSciences) and 10× minimum staple excess with a 10 nM scaffold concentration in 100 mM tris-HCl, 10 mM EDTA (pH 8.0), and 12 mM $MgCl_2$. Samples were annealed in a thermocycler (Eppendorf Mastercycler Nexus), holding at 65°C for 15 min followed by linear cooling from 50° to 40°C over 18 hours.

Gel electrophoresis of DNA voxels

Agarose gel electrophoresis (Thermo Fisher Scientific, EasyCast Mini Gel Electrophoresis System) was used to purify monomers. The gel contained 1.95 g of agarose powder (Bioline, final concentration: 1.3% w/v) in 150 ml of a 0.5× TBE buffer [50 mM Tris, 50 mM boric acid, 1 mM EDTA, and 11 mM $MgCl_2$ (pH 8.3)] and 3 μl of SYBR Safe (Thermo Fisher Scientific). Gels were run at 70 V for ~2 to 3 hours at room temperature. A 1-kb ladder (catalog no. N0552S, Biolabs) or 1-kb plus ladder (catalog no. 10787018, Thermo Fisher Scientific) was used. Data file S2 gives conditions for all gels. Gel images were captured using a Bio-Rad ChemiDoc imaging system with either the Cy3 or SYBR Safe filter setting. Gel image analysis and band densitometry were carried out using the Bio-Rad Image Lab software. Bands of interest were excised on a blue light transilluminator (Fisher Biotec) and extracted using a spin filter (Bio-Rad, Freeze 'N Squeeze column) at 18,000*g* and 4°C for 20 min. The concentration of DNA was measured on a NanoDrop spectrophotometer (Thermo Fisher Scientific).

Voxel purification using PEG precipitation

PEG precipitation was used to concentrate gel-purified monomers and to remove excess staples. Mg^{2+} was increased to 20 mM by adding an appropriate amount of 1 M $MgCl_2$. An equal volume of the DNA sample and a 2× PEG buffer [15% 8000 PEG (w/v), 5 mM Tris, 1 mM EDTA, and 505 mM NaCl] were mixed, briefly vortexed, and then centrifuged at 16,000*g* and 25°C for 25 min. The supernatant was removed using a pipette, and the pellet was resuspended in 15 μl of 1× TE (5 mM tris, 1 mM EDTA) and 10 mM $MgCl_2$ for 3 hours at 30°C on a shaker at 1000 rpm.

Voxel purification using ultracentrifugation

To purify monomers, we used the rate-zonal centrifugation protocol with a 15 to 45% (v/v) glycerol gradient (*59*). A commercial Gradient Station (BIOCOMP) unit was used to prepare the glycerol gradient by gently rotating a compatible tube containing two layers of 15% glycerol followed by 45% (1× TE and 10 mM $MgCl_2$) at 20 rpm and 85°C for 1 min. The glycerol gradient was spun in a Beckman SW55-Ti rotor at 55,000 rpm and 4°C for 45 min. The gradient was fractionated into 100-μl fractions using an automated Gradient Station equipped with ultraviolet absorbance detection at 260 nm (BIOCOMP). For large assemblies, a 12-ml tube with an SW41 rotor was used for gradient purification. Conditions were rotation at 15 rpm and 81.5°C for 2.5 min for gradient formation and then ultracentrifugation at 41,000 rpm and 4°C for 25 min. Fractions were loaded into an agarose gel to resolve the content and determine fractions with DNA. PEG precipitation was used to exchange a glycerol buffer to 1× TE and 10 mM $MgCl_2$ buffer for TEM. Typical fluorescent traces from fractionation are shown in figs. S81 to S83.

Multicomponent assembly

Unique monomers were folded in separate tubes. The relative folding yield was determined by comparing the band intensity in the agarose gel. Unpurified monomers were pooled with an appropriate volume accounting for the relative folding yield to give equal monomer concentrations. Monomer pools were purified by either gel or ultracentrifugation, and PEG was precipitated to obtain purified and concentrated monomer pools (table S10). Unoptimized yields from the M13 scaffold to the purified monomer pool were 6% by gel purification or 40% by gradient ultracentrifugation (fig. S81). Some assembly reactions used unpurified monomer pools or only PEG precipitation to concentrate and remove excess staples. Purification methods used for each sample are summarized in data file S2. For assembly, monomer pools were mixed with intra- and intermonomer connector strands, 1× TE buffer, and 1 M $MgCl_2$ to obtain a solution containing 1 nM per unique monomer, 200-nM connector strands, 1× TE, and 20 mM Mg^{2+}. Additional intramonomer connectors were added to ensure monomer stability. Samples were incubated in a thermocycler at 40°C for 18 hours.

Negative-stain TEM and analysis

For TEM imaging, a plasma-treated grid with Formvar film and heavy carbon coating (Ted Pella EM grids, GSCU300CH-50) was used. A 5-μl sample was incubated on the grid for 1 to 10 min. Excess sample was blotted off with filter paper; 10 μl of 2% uranyl acetate in water was added to the grid and then blotted immediately on filter paper. TEM images were acquired on a JEOL 1400 TEM in bright-field mode with 120-kV accelerating voltage.

2D particle class averages were derived from TEM micrographs using RELION (*60*). Particle picking and 2D classification were performed with an automated particle picking algorithm (Laplacian-of-Gaussian, RELION 3.0.6) for small assemblies (monomer, dimer, and trimer) and manual picking for larger structures. The number of nonzero classes in RELION 2D classification was low ($n = 1$ to 4) and typically showed distinct particle orientations (top, side, and reflected). To give an unbiased assessment of particle homogeneity, we ensured that no particles were discarded, and all class averages are shown in the supplementary figures. Autopicking occasionally resulted in artifacts from selection of text annotation in TEM images (e.g., fig. S43). Some larger shapes required uniform particle orientation in images for determination of accurate 2D class averages. To achieve this, we manually rotated TEM images before the RELION workflow. Class averages were used for yield calculations. Persistence lengths for coaxial and lateral polymers were determined using a MATLAB script from a published method (*61*).

Cryo-EM imaging and particle reconstruction

Cryo-EM single-particle analysis was used to determine structural details of monomers. Sample conditions were 3 μl, 700 nM nanostructure, and 1× TE buffer with 6 mM $MgCl_2$. Specimens were prepared on C-flat grids (ProSciTech) after plasma cleaning using a Gantan Solarus plasma cleaner. Subsequently, grids were plunge-frozen using a Vitrobot Mark IV. Grids were then loaded into a

Thermo Fisher Scientific Glacios Cryo-EM equipped with a 200-kV field-emission gun source.

Data acquisition was conducted on a Falcon 2 direct electron detector, with the Thermo Fisher Scientific EPU software automating the data collection process. The magnification and electron dose were set for the dataset in Fig. 1C (ii) such that the pixel resolution was 1.1 Å per pixel and the electron dose was 40 electrons/Å^2; for all other cryo-EM models, the pixel resolution was 0.86 Å per pixel, and the electron dose was 50 electrons/Å^2.

The subsequent image processing workflow was executed using the CryoSPARC (v4) for particle picking, 2D classification, and 3D reconstruction. Initially, a small subset of the micrograph dataset was selected for manual particle picking, followed by 2D classification and 3D reconstruction. After that, the 3D model was used to generate 50 templates, showing possible orientations of particles in the ice. These preliminary templates were then used for automated particle picking from all micrographs. Picked points were inspected and filtered by changing the power score and normalized cross-correlation score to remove empty areas. The particles were then subjected to 2D classification, allowing for the refinement of particle groups on the basis of structural similarities. These averages served as the foundation for the 3D reconstruction process, ultimately yielding detailed and informative 3D models of the monomers.

Super-resolution fluorescent microscopy (DNA-PAINT)

A total internal reflectance fluorescence microscope (Oxford Nanoimager) was used to perform DNA-PAINT imaging. Samples were prepared following a literature protocol (*62*) that included addition of a DNA origami tile as a fiducial marker. Sample conditions were 0.25 nM DNA barrel monomer, 0.25 nM DNA origami tile, and 5 nM imager strand with Cy3B fluorophore. Imaging parameters consisted of 70-mW laser power and 300-ms exposure time in total internal reflection mode. The localization of fluorophore binding sites was analyzed using the DNA-PAINT software (Picasso), which processed 5000 to 10,000 time-lapsed images. Typical parameters in Picasso included baseline (400), sensitivity (0.47), quantum efficiency (0.8), and pixel size (117 nm).

Switching monomers between coaxial and lateral states

Monomers were folded and gel-purified. To switch between the two structures, we added lateral invader and coaxial connector strands to the purified lateral monomer and coaxial invader and lateral connectors to the purified coaxial monomer. Concentrations used for the switching reactions were 0.5 nM monomer, 100 nM connectors, 100 nM invaders, and 20 mM Mg^{2+}. Switching samples were incubated at 40°C for 18 hours before TEM analysis.

Multistep assembly of the swirl and 28-monomer rectangle

The 8-monomer swirl is a homodimer of two 4-monomer subunits. In stage one, purified and concentrated monomers were used to construct a 4-monomer subunit. In stage two, 4-monomer subunits were gel-purified, and connector strands for dimerization were added and then incubated at 38°C for 18 hours. The concentration values used were as follows: 0.01 nM 4-monomer subunit, 200 nM connector strands (intra and inter), and 20 mM Mg^{2+}. The 28-monomer rectangle was assembled using two 8-monomer and two 6-monomer subunits in stage one. In stage two, subunits were purified and combined, and connector strands were added. The solution was annealed from 40° to 30°C for 18 hours. The concentration values used were 0.065 nM per subunit, 40 nM connector strands (intra and inter), and 40 mM Mg^{2+}.

DNA-PAINT imaging of dinosaur assembly

The slide protocol was modified to increase the nanostructure incubation time to 10 min given the low sample concentration. For one sample, 5 μl of the unpurified dinosaur assembly mixture was added to 3.18 μl of 1.57 nM gel-purified DNA tile, 2 μl of 0.5% Tween 20, and 9.82 μl of 1× TE and 10 mM Mg^{2+}. Imaging parameters as in the method described above were used to acquire 10,000 time-lapsed images.

Assembly pathways

In step one, initial states were assembled from monomers and used either unpurified or gel purified. For subsequent steps, additional connector strands were added. Typical values were 200 nM connectors to 0.05 to 0.008 nM assembly in 20 mM Mg^{2+} incubated at 40°C for 18 hours. Assembly conditions for each design are reported in data file S2.

Reconfiguration

To perform reconfiguration, we assembled the first state, gel-purified it, and then incubated with connector and invader strands. Typical conditions used were 0.05 nM initial structure, 200 nM invader and connector strands, and 20 mM Mg^{2+} for 6 hours at 37°C. Connector and invader concentrations were selected to maintain a concentration in the range of 50 to 400 nM for prototyping reconfiguration reactions but were not optimized.

Time-resolved reconfiguration

Multiple aliquots of purified structures were prepared, and connector and invader strands were added to each aliquot at time intervals of 0, 10, 20, 40 and 60 min. The mixtures were incubated at 40°C at concentrations of 0.07 nM rod structure, 200 nM connector and invader strands, and 20 mM Mg^{2+} in a 25-μl aliquot. After incubation, aliquots were immediately placed in dry ice to stop the assembly. To prepare the TEM grids, we defrosted frozen samples by adding 20 μl of 1× TE to the 25-μl aliquot and quickly mixing with a pipette. The percentage of correctly switched particles was determined from TEM images and used to calculate the reaction rate constant, assuming a second-order reaction.

Multiple reconfiguration cycles

Five complete switching cycles, equivalent to 10 switching steps, were performed for 18 hours at 40°C for each step. Using the same batch of the starting material, 10 × 20-μl aliquots were prepared. Initial conditions were 0.08 nM flexible chain, connector = 50 nM, and invader = 50 nM. In each switching step, the same connector and invader solution was added to all aliquots to trigger switching. In addition, one aliquot was reserved and stored at −20°C and imaged using TEM to determine the switching yield for that step. It was necessary to add increasing amounts of connector and invader strands to achieve high switching yields (fig. S58). For each switching step, the required amount of connector strand was added to achieve a constant concentration ratio of connector:invader of 2.3. Connector concentrations for steps 1 to 10 were 50, 110, 215, 330, 512, 678, 917, 1082, 1309, and 1411 nM. Invader concentrations were 50, 48, 93, 143, 223, 295, 400, 470, 570, and 614 nM.

Gold nanoparticle conjugation

Citrate-coated gold nanoparticles (10 and 20 nm) were prestabilized with 4,4′-(phenylphosphinidene)bis(benzenesulfonic acid) dipotassium salt hydrate. Dithiol DNA purchased from IDT and added in 300× excess to phosphine-coated gold with 100 mM NaCl and incubated at 25°C for 18 hours and then purified and concentrated using a Millipore Amicon filter (50K) with three washes of a 1× TE buffer. Incubation concentrations of gold and DNA were 0.11 and 36 mM. To combine the gold nanoparticle–DNA complex with the nanostructure, we mixed the samples at a 1:20 molar ratio and incubated at 40°C for 18 hours.

Statistical tests

The mean and SD were used for statistical analysis to quantify the assembly yield and precision using descriptive statistical functions in Excel. Gel electrophoresis results were used to quantify the assembly yield, whereas wide-field TEM was used to assess structural accuracy. The statistical data in Fig. 2 (C and D) show an analysis of assembly precision, determined by quantifying structural discrepancies in a population of n assemblies, as observed in wide-field TEM micrographs and compared with model predictions. The statistical data in Fig. 3D present an analysis of the relationship between the assembly size and yield for N independent designs, calculated using gel electrophoresis results from figs. S17, S18, S25, S27 to S33, S40, S41, and S44. The statistical data in Fig. 5A show the yield of different assembly pathways, calculated using gel electrophoresis results from fig. S66.

Supplementary Materials

The PDF file includes:
Discussions S1 to S4
Figs. S1 to S97
Tables S1 to S10

Other Supplementary Material for this manuscript includes the following:
Data files S1 and S2
MDAR Reproducibility Checklist

REFERENCES AND NOTES

1. G. M. Whitesides, B. Grzybowski, Self-assembly at all scales. *Science* **295**, 2418–2421 (2002).
2. J. W. Szostak, D. P. Bartel, P. L. Luisi, Synthesizing life. *Nature* **409**, 387–390 (2001).
3. B. L. Feringa, The art of building small: From molecular switches to motors (Nobel Lecture). *Angew. Chem. Int. Ed. Engl.* **56**, 11060–11078 (2017).
4. G. M. Whitesides, J. P. Mathias, C. T. Seto, Molecular self-assembly and nanochemistry: A chemical strategy for the synthesis of nanostructures. *Science* **254**, 1312–1319 (1991).
5. Z. Chen, R. D. Kibler, A. Hunt, F. Busch, J. Pearl, M. Jia, Z. L. VanAernum, B. I. M. Wicky, G. Dods, H. Liao, M. S. Wilken, C. Ciarlo, S. Green, H. El-Samad, J. Stamatoyannopoulos, V. H. Wysocki, M. C. Jewett, S. E. Boyken, D. Baker, De novo design of protein logic gates. *Science* **368**, 78–84 (2020).
6. I. D. Lutz, S. Wang, C. Norn, A. Courbet, A. J. Borst, Y. T. Zhao, A. Dosey, L. Cao, J. Xu, E. M. Leaf, C. Treichel, P. Litvicov, Z. Li, A. D. Goodson, P. Rivera-Sánchez, A. M. Bratovianu, M. Baek, N. P. King, H. Ruohola-Baker, D. Baker, Top-down design of protein architectures with reinforcement learning. *Science* **380**, 266–273 (2023).
7. J. Zheng, J. J. Birktoft, Y. Chen, T. Wang, R. Sha, P. E. Constantinou, S. L. Ginell, C. Mao, N. C. Seeman, From molecular to macroscopic via the rational design of a self-assembled 3D DNA crystal. *Nature* **461**, 74–77 (2009).
8. S. M. Douglas, I. Bachelet, G. M. Church, A logic-gated nanorobot for targeted transport of molecular payloads. *Science* **335**, 831–834 (2012).
9. A. Gopinath, E. Miyazono, A. Faraon, P. W. K. Rothemund, Engineering and mapping nanocavity emission via precision placement of DNA origami. *Nature* **535**, 401–405 (2016).
10. A.-K. Pumm, W. Engelen, E. Kopperger, J. Isensee, M. Vogt, V. Kozina, M. Kube, M. N. Honemann, E. Bertosin, M. Langecker, R. Golestanian, F. C. Simmel, H. Dietz, A DNA origami rotary ratchet motor. *Nature* **607**, 492–498 (2022).
11. A. Michelson, B. Minevich, H. Emamy, X. Huang, Y. S. Chu, H. Yan, O. Gang, Three-dimensional visualization of nanoparticle lattices and multimaterial frameworks. *Science* **376**, 203–207 (2022).
12. E. Benson, R. C. Marzo, J. Bath, A. J. Turberfield, A DNA molecular printer capable of programmable positioning and patterning in two dimensions. *Sci. Robot.* **7**, eabn5459 (2022).
13. S. Romero-Romero, S. Kordes, F. Michel, B. Höcker, Evolution, folding, and design of TIM barrels and related proteins. *Curr. Opin. Struct. Biol.* **68**, 94–104 (2021).
14. K. A. Dill, J. L. MacCallum, The protein-folding problem, 50 years on. *Science* **338**, 1042–1046 (2012).
15. D. Baker, What has de novo protein design taught us about protein folding and biophysics? *Protein Sci.* **28**, 678–683 (2019).
16. A. C. Apetri, A. L. Horwich, Chaperonin chamber accelerates protein folding through passive action of preventing aggregation. *Proc. Natl. Acad. Sci. U.S.A.* **105**, 17351–17355 (2008).
17. I. Kostitsyna, C. Wood, D. Woods, Turning machines: A simple algorithmic model for molecular robotics. *Nat. Comput.* **23**, 407–430 (2022).
18. D. Woods, D. Doty, C. Myhrvold, J. Hui, F. Zhou, P. Yin, E. Winfree, Diverse and robust molecular algorithms using reprogrammable DNA self-assembly. *Nature* **567**, 366–372 (2019).
19. P. W. K. Rothemund, N. Papadakis, E. Winfree, Algorithmic self-assembly of DNA Sierpinski triangles. *PLOS Biol.* **2**, e424 (2004).
20. G. Tikhomirov, P. Petersen, L. Qian, Fractal assembly of micrometre-scale DNA origami arrays with arbitrary patterns. *Nature* **552**, 67–71 (2017).
21. S. F. J. Wickham, A. Auer, J. Min, N. Ponnuswamy, J. B. Woehrstein, F. Schueder, M. T. Strauss, J. Schnitzbauer, B. Nathwani, Z. Zhao, S. D. Perrault, J. Hahn, S. Lee, M. M. Bastings, S. W. Helmig, A. L. Kodal, P. Yin, R. Jungmann, W. M. Shih, Complex multicomponent patterns rendered on a 3D DNA-barrel pegboard. *Nat. Commun.* **11**, 5768 (2020).
22. G. Yao, F. Zhang, F. Wang, T. Peng, H. Liu, E. Poppleton, P. Šulc, S. Jiang, L. Liu, C. Gong, X. Jing, X. Liu, L. Wang, Y. Liu, C. Fan, H. Yan, Meta-DNA structures. *Nat. Chem.* **12**, 1067–1075 (2020).
23. Y. He, T. Ye, M. Su, C. Zhang, A. E. Ribbe, W. Jiang, C. Mao, Hierarchical self-assembly of DNA into symmetric supramolecular polyhedra. *Nature* **452**, 198–201 (2008).
24. C. G. Evans, J. O'Brien, E. Winfree, A. Murugan, Pattern recognition in the nucleation kinetics of non-equilibrium self-assembly. *Nature* **625**, 500–507 (2024).
25. A. M. Mohammed, P. Šulc, J. Zenk, R. Schulman, Self-assembling DNA nanotubes to connect molecular landmarks. *Nat. Nanotechnol.* **12**, 312–316 (2017).
26. C. M. Wintersinger, D. Minev, A. Ershova, H. M. Sasaki, G. Gowri, J. F. Berengut, F. E. Corea-Dilbert, P. Yin, W. M. Shih, Multi-micron crisscross structures grown from DNA-origami slats. *Nat. Nanotechnol.* **18**, 281–289 (2023).
27. J. Song, Z. Li, P. Wang, T. Meyer, C. Mao, Y. Ke, Reconfiguration of DNA molecular arrays driven by information relay. *Science* **357**, eaan3377 (2017).
28. M. Kim, C. Lee, K. Jeon, J. Y. Lee, Y. J. Kim, J. G. Lee, H. Kim, M. Cho, D. N. Kim, Harnessing a paper-folding mechanism for reconfigurable DNA origami. *Nature* **619**, 78–86 (2023).
29. K. F. Wagenbauer, C. Sigl, H. Dietz, Gigadalton-scale shape-programmable DNA assemblies. *Nature* **552**, 78–83 (2017).
30. J. F. Berengut, C. K. Wong, J. C. Berengut, J. P. K. Doye, T. E. Ouldridge, L. K. Lee, Self-limiting polymerization of DNA origami subunits with strain accumulation. *ACS Nano* **14**, 17428–17441 (2020).
31. P. W. K. Rothemund, Folding DNA to create nanoscale shapes and patterns. *Nature* **440**, 297–302 (2006).
32. S. M. Douglas, H. Dietz, T. Liedl, B. Högberg, F. Graf, W. M. Shih, Self-assembly of DNA into nanoscale three-dimensional shapes. *Nature* **459**, 414–418 (2009).
33. J. B. Knudsen, L. Liu, A. L. Bank Kodal, M. Madsen, Q. Li, J. Song, J. B. Woehrstein, S. F. J. Wickham, M. T. Strauss, F. Schueder, J. Vinther, A. Krissanaprasit, D. Gudnason, A. A. A. Smith, R. Ogaki, A. N. Zelikin, F. Besenbacher, V. Birkedal, P. Yin, W. M. Shih, R. Jungmann, M. Dong, K. V. Gothelf, Routing of individual polymers in designed patterns. *Nat. Nanotechnol.* **10**, 892–898 (2015).
34. W. Liu, J. Halverson, Y. Tian, A. V. Tkachenko, O. Gang, Self-organized architectures from assorted DNA-framed nanoparticles. *Nat. Chem.* **8**, 867–873 (2016).
35. I. Smyrlaki, F. Fördős, I. Rocamonde-Lago, Y. Wang, B. Shen, A. Lentini, V. C. Luca, B. Reinius, A. I. Teixeira, B. Högberg, Soluble and multivalent Jag1 DNA origami nanopatterns activate Notch without pulling force. *Nat. Commun.* **15**, 465 (2024).
36. R. Dong, T. Aksel, W. Chan, R. N. Germain, R. D. Vale, S. M. Douglas, DNA origami patterning of synthetic T cell receptors reveals spatial control of the sensitivity and kinetics of signal activation. *Proc. Natl. Acad. Sci. U.S.A.* **118**, e2109057118 (2021).
37. E. Kopperger, J. List, S. Madhira, F. Rothfischer, D. C. Lamb, F. C. Simmel, A self-assembled nanoscale robotic arm controlled by electric fields. *Science* **359**, 296–301 (2018).

38. N. Sarraf, K. R. Rodriguez, L. Qian, Modular reconfiguration of DNA origami assemblies using tile displacement. *Sci. Robot.* **8**, eadf1511 (2023).
39. A. E. Marras, L. Zhou, H.-J. Su, C. E. Castro, Programmable motion of DNA origami mechanisms. *Proc. Natl. Acad. Sci. U.S.A.* **112**, 713–718 (2015).
40. T. Gerling, K. F. Wagenbauer, A. M. Neuner, H. Dietz, Dynamic DNA devices and assemblies formed by shape-complementary, non–base pairing 3D components. *Science* **347**, 1446–1452 (2015).
41. A. Gopinath, C. Thachuk, A. Mitskovets, H. A. Atwater, D. Kirkpatrick, P. W. K. Rothemund, Absolute and arbitrary orientation of single-molecule shapes. *Science* **371**, eabd6179 (2021).
42. Z. Lin, H. Emamy, B. Minevich, Y. Xiong, S. Xiang, S. Kumar, Y. Ke, O. Gang, Engineering organization of DNA nano-chambers through dimensionally controlled and multi-sequence encoded differentiated bonds. *J. Am. Chem. Soc.* **142**, 17531–17542 (2020).
43. Y. Zhou, J. Dong, C. Zhou, Q. Wang, Finite assembly of three-dimensional DNA hierarchical nanoarchitectures through orthogonal and directional bonding. *Angew. Chem. Int. Ed. Engl.* **61**, e202116416 (2022).
44. Y. Ke, L. L. Ong, W. M. Shih, P. Yin, Three-dimensional structures self-assembled from DNA bricks. *Science* **338**, 1177–1183 (2012).
45. Z. Zhao, M. Zhang, J. M. Hogle, W. M. Shih, G. Wagner, M. L. Nasr, DNA-corralled nanodiscs for the structural and functional characterization of membrane proteins and viral entry. *J. Am. Chem. Soc.* **140**, 10639–10643 (2018).
46. J. Hahn, L. Y. T. Chou, R. S. Sørensen, R. M. Guerra, W. M. Shih, Extrusion of RNA from a DNA-origami-based nanofactory. *ACS Nano* **14**, 1550–1559 (2020).
47. S. M. Douglas, A. H. Marblestone, S. Teerapittayanon, A. Vazquez, G. M. Church, W. M. Shih, Rapid prototyping of 3D DNA-origami shapes with caDNAno. *Nucleic Acids Res.* **37**, 5001–5006 (2009).
48. P. Šulc, F. Romano, T. E. Ouldridge, L. Rovigatti, J. P. K. Doye, A. A. Louis, Sequence-dependent thermodynamics of a coarse-grained DNA model. *J. Chem. Phys.* **137**, 135101 (2012).
49. E. Poppleton, M. Matthies, D. Mandal, F. Romano, P. Šulc, L. Rovigatti, oxDNA: Coarse-grained simulations of nucleic acids made simple. *J. Open Source Softw.* **8**, 4693 (2023).
50. C. Lee, K. S. Kim, Y.-J. Kim, J. Y. Lee, D.-N. Kim, Tailoring the mechanical stiffness of DNA nanostructures using engineered defects. *ACS Nano* **13**, 8329–8336 (2019).
51. D. Y. Zhang, G. Seelig, Dynamic DNA nanotechnology using strand-displacement reactions. *Nat. Chem.* **3**, 103–113 (2011).
52. E. D. Demaine, M. L. Demaine, S. P. Fekete, M. Ishaque, E. Rafalin, R. T. Schweller, D. L. Souvaine, "Staged self-assembly: Nanomanufacture of arbitrary shapes with O(1) glues" in *DNA Computing. DNA 2007. Lecture Notes in Computer Science*, M. H. Garzon, H. Yan, Eds. (Springer, 2008), vol. 4848, pp. 1–14.
53. F. Schneider, N. Möritz, H. Dietz, The sequence of events during folding of a DNA origami. *Sci. Adv.* **5**, eaaw1412 (2019).
54. M. DeLuca, D. Duke, T. Ye, M. Poirier, Y. Ke, C. Castro, G. Arya, Mechanism of DNA origami folding elucidated by mesoscopic simulations. *Nat. Commun.* **15**, 3015 (2024).
55. M. T. Strauss, F. Schueder, D. Haas, P. C. Nickels, R. Jungmann, Quantifying absolute addressability in DNA origami with molecular resolution. *Nat. Commun.* **9**, 1600 (2018).
56. N. Ponnuswamy, M. M. C. Bastings, B. Nathwani, J. H. Ryu, L. Y. T. Chou, M. Vinther, W. A. Li, F. M. Anastassacos, D. J. Mooney, W. M. Shih, Oligolysine-based coating protects DNA nanostructures from low-salt denaturation and nuclease degradation. *Nat. Commun.* **8**, 15654 (2017).
57. A. S. Eklund, A. Comberlato, I. A. Parish, R. Jungmann, M. M. C. Bastings, Quantification of strand accessibility in biostable DNA origami with single-staple resolution. *ACS Nano* **15**, 17668–17677 (2021).
58. S. I. S. Hendrikse, N. Todorova, H. Soleimaninejad, P. Charchar, M. A. Sani, K. al Taief, J. F. Berengut, S. F. J. Wickham, S. L. Gras, A. C. Fahrenbach, P. Thordarson, A. V. Ellis, Exploring artificial nucleic acid mimicking peptide nanofibers. *Chem. Mater.* **35**, 4355–4365 (2023).
59. C. Lin, S. D. Perrault, M. Kwak, F. Graf, W. M. Shih, Purification of DNA-origami nanostructures by rate-zonal centrifugation. *Nucleic Acids Res.* **41**, e40 (2013).
60. S. H. W. Scheres, RELION: Implementation of a Bayesian approach to cryo-EM structure determination. *J. Struct. Biol.* **180**, 519–530 (2012).
61. R. Jurado, J. Adamcik, A. Sánchez-Ferrer, S. Bolisetty, R. Mezzenga, N. Gálvez, Understanding the formation of apoferritin amyloid fibrils. *Biomacromolecules* **22**, 2057–2066 (2021).
62. J. Schnitzbauer, M. T. Strauss, T. Schlichthaerle, F. Schueder, R. Jungmann, Super-resolution microscopy with DNA-PAINT. *Nat. Protoc.* **12**, 1198–1228 (2017).

Acknowledgments: We thank the Australian Microscopy & Microanalysis Research Facility (ammrf.org.au) node at the University of Sydney: Sydney Microscopy & Microanalysis and Sydney Analytical, a core research facility at the University of Sydney for the facilities as well as the scientific and technical assistance. **Funding:** This work was supported by the Australian Research Council (ARC) [DE180101635 (S.F.J.W.) and DP210101892 (S.M.)]; Westpac Research Fellowship (S.F.J.W., K.C.D.G., and M.T.L.); University of Sydney, University of Sydney Nano Institute (J.F.B., M.T.L., and J.K.D.S.), and University of Sydney Physics Foundation (M.T.L.); Australian Postgraduate Award (M.T.L., J.K.D.S., and M.T.); Australian Department of Industry, Science, Energy and Resources AUSMURIV000001 (M.T.L., J.-B.C., and J.L.); and the Engineering and Physical Sciences Research Council (EPSRC) [EP/L015722/1 (H.F.)]. **Author contributions:** M.T.L. and J.F.B. designed and performed research and analyzed and discussed data. J.L. and J.-B.C. performed research and analyzed data. J.K.D.S., K.C.D.G., M.T., K.S., S.M., and W.C. performed research. H.F. and J.P.K.D. performed research and analyzed and discussed data. A.A. analyzed and discussed data. S.F.J.W. designed and analyzed and discussed data. M.T.L. and S.F.J.W. wrote the manuscript. All authors edited the manuscript. **Competing interests:** The authors declare that they have no competing interests. **Data and materials availability:** All data needed to evaluate the conclusions in the paper are present in the paper or the Supplementary Materials. Extended data files and scripts, including the caDNAno design file, for this study have been deposited in the Figshare database: https://doi.org/10.6084/m9.figshare.27208434.v5.

Submitted 14 March 2024
Accepted 30 October 2024
Published 27 November 2024
10.1126/scirobotics.adp2309

Science Robotics

Reconfigurable nanomaterials folded from multicomponent chains of DNA origami voxels

Minh Tri Luu, Jonathan F. Berengut, Jiahe Li, Jing-Bing Chen, Jasleen Kaur Daljit Singh, Kanako Coffi Dit Glieze, Matthew Turner, Karuna Skipper, Sreelakshmi Meppat, Hannah Fowler, William Close, Jonathan P. K. Doye, Ali Abbas, and Shelley F. J. Wickham

Sci. Robot. **9** (96), eadp2309. DOI: 10.1126/scirobotics.adp2309

Editor's summary

The development of synthetic molecular structures that can self-assemble into unique complex machines is a challenge. Inspired by protein folding, Luu *et al.* have developed a modular system of origami voxels made from DNA nanostructures. These voxels contain internal and external connections that can be switched between various states. They can be combined to form two-dimensional and three-dimensional hierarchical assemblies and be reconfigured into new shapes. The modular system could potentially be adapted for environment-adaptive switching and reconfiguration in response to temperature and pH. —Amos Matsiko